# Absolute frequency measurements on the 2S → 3S transition of lithium-6,7

**Rodolfo Sánchez**[1,5], **Monika Žáková**[2], **Zoran Andjelkovic**[2], **Bruce A Bushaw**[3], **Kamalesh Dasgupta**[4], **Guido Ewald**[1], **Christopher Geppert**[1,2], **H-Jürgen Kluge**[1], **Jörg Krämer**[2], **Matthias Nothhelfer**[2], **Dirk Tiedemann**[2], **Danyal F A Winters**[1] **and Wilfried Nörtershäuser**[1,2]

[1] GSI Helmholtzzentrum für Schwerionenforschung GmbH, Planckstrasse 1, D-64291 Darmstadt, Germany
[2] Institut für Kernchemie, Johannes Gutenberg-Universität Mainz, Fritz-Straßman-Weg 2, D-55128 Mainz, Germany
[3] Chemical Sciences Division, Pacific Northwest National Laboratory, Richland, WA 99352, USA
[4] Bhabha Atomic Research Center, Mumbai 400085, India
E-mail: R.Sanchez@gsi.de

**Abstract.** The frequencies of the 2S–3S two-photon transition for the stable lithium isotopes were measured by cavity-enhanced Doppler-free laser excitation that was controlled by a femtosecond frequency comb. The resulting values of 815 618 181.57(18) and 815 606 727.59(18) MHz, respectively, for $^7$Li and $^6$Li are in agreement with previous measurements but are more accurate by an order of magnitude. There is still a discrepancy of about 11.6 and 10.6 MHz from the latest theoretical values. This is comparable to the uncertainty in the theoretical calculations, while uncertainty in our experimental values is more than a hundred-fold smaller. More accurate theoretical calculation of the transition frequencies would allow extraction of the absolute charge radii for these stable isotopes, which in turn could improve nuclear charge radii values for the unstable lithium isotopes.

[5] Author to whom any correspondence should be addressed.

**IOP** Institute of Physics $\Phi$ DEUTSCHE PHYSIKALISCHE GESELLSCHAFT

## Contents

## 1. Introduction

The binding energy of an atomic state is one of the most fundamental quantities in quantum mechanics. Experiments can nowadays reach accuracy levels sufficient to extract improved values of fundamental constants like the fine structure constant $\alpha$ or to probe the structure of the nucleus. Even though the nucleus is five orders of magnitude smaller than the atom, its finite size significantly alters atomic energy levels. A second effect that can alter the energy level is the electric polarizability of the nucleus. This contribution is usually on the kHz scale but for exotic nuclei with large $B(E1)$ linestrength this effect can be larger. The contribution has been recently calculated for the first time for a halo nucleus and was found to contribute with 39 kHz to the isotope shift between $^9$Li and $^{11}$Li [1]. Calculations for $^{11}$Be, the nucleus with the largest known $B(E1)$ strength, give a contribution of 208(21) kHz [2].

A complete treatment of level energies and isotope shifts requires the consideration of non-relativistic, relativistic, quantum electrodynamical (QED) and nuclear structure contributions. The non-relativistic energies and lowest-order relativistic corrections can now be calculated to spectroscopic accuracy [2]–[7], but the QED corrections still limit the overall accuracy. One of the main difficulties and long-standing problems was the calculation of the so-called Bethe logarithm, which is the dominant part of the electron self-energy. Its calculation for hydrogen-like [8] and helium-like systems [9] was recently followed by the report of the complete calculation of QED terms up to the order of $\alpha^3$ Ry [2, 7, 10] for lithium atoms. In [10] Yan and Drake calculated the Bethe logarithm $\ln k_0$ to a relative accuracy of $10^{-6}$, and in [11] Pachucki reports on the Bethe logarithm of the four-electron system beryllium with a relative accuracy of $10^{-5}$.

The main motivation of these theoretical works was the accurate determination of the mass-dependent terms in the transition energies that lead to the so-called mass shift in the transition frequencies between different isotopes of the same element. Accurately calculated mass shifts play a key role in several experiments that determine the charge radius of halo isotopes, which have been carried out recently [12]–[17] or are planned for the near future [18, 19]. In these experiments, the change in the transition frequency between the isotopes $A$

**Table 1.** Contributions of the various expansive terms to the absolute 2S–3S transition energy in $^7$Li. All values are in given MHz. Values from [2] are based on table III in this reference.

| Term | Yan *et al* [7] [a] | Puchalski and Pachucki [2] |
|------|---------------------|----------------------------|
| $E_{\mathrm{NR}}$ | $815\,561\,313.44 \pm 0.03$ | $815\,561\,313.5 \pm 0.1$ |
| $E_{\mathrm{Rel}}$ | $62\,629.4 \pm 0.6$ | $62\,628.0 \pm 0.7$ |
| $E_{\mathrm{QED}}$ | $-5768 \pm 30$ | $-5763 \pm 19$ |
| $E_{\mathrm{FS}}$ | $-8.95 \pm 0.24$ | $-8.9 \pm 0.2$ |
| Total | $815\,618\,166 \pm 30$ | $815\,618\,170 \pm 19$ |

[a] Erratum submitted to *Phys. Rev. Lett.*

and $A'$ (the isotope shift $\delta\nu^{A,A'}$) was accurately measured. After subtracting the calculated mass-dependent shift, the so-called field shift is obtained, which is due to the change in the nuclear charge distribution between the isotopes $A$ and $A'$. This field shift is sensitive to $\delta\langle r^2 \rangle^{A,A'}$, i.e. the change in the mean-square nuclear charge radius. To determine the charge radii in a series of isotopes, a reference charge radius has to be measured using a different method, e.g. electron scattering. Unfortunately, these scattering experiments are usually much less accurate than optical measurements and the uncertainty of the reference radius often dominates the final uncertainty of the nuclear charge radii. Thus, it would be very advantageous if the total charge radius of an isotope could be extracted directly from optical measurements. In principle, this should be possible because the transition frequency carries information about the total nuclear charge radius. The total energy of an atomic state is usually expanded in the form

$$E = E_{\mathrm{NR}} + E_{\mathrm{Rel}} + E_{\mathrm{QED}} + E_{\mathrm{FS}}, \tag{1}$$

where $E_{\mathrm{NR}}$ is the non-relativistic energy, $E_{\mathrm{Rel}}$ is the relativistic correction, $E_{\mathrm{QED}}$ is the QED shift and $E_{\mathrm{FS}}$ is the finite nuclear size correction. The most accurate treatments available solve the non-relativistic Schrödinger equation variationally in multiple-basis sets in Hylleraas coordinates [10, 11] and use the resulting wave functions to calculate relativistic and QED corrections perturbatively. Table 1, summarized from [2, 7, 20], lists the different contributions to the $1s^2\, 2s\, ^2S_{1/2} - 1s^2\, 3s\, ^2S_{1/2}$ transitions in $^7$Li. The non-relativistic contributions include the first- and second-order mass polarization term. $E_{\mathrm{Rel}}$ are the lowest-order $\alpha^2$ Ry relativistic corrections from the Breit–Pauli interaction, including the first-order mass polarization term, and $E_{\mathrm{QED}}$ include the lowest-order $\alpha^3$ Ry electron–nucleus and electron–electron terms, and higher-order terms of $O(\alpha^4 \mathrm{Ry})$ and higher. The total transition energy deviates from the value reported in [7] because instead of using the Bethe logarithm reported in table I in [7] for calculating the transition frequency, an obsolete value from [10] has been used erroneously.

The nuclear size contribution $E_{\mathrm{FS}}$ has been calculated using a $^7$Li charge radius of 2.39(3) fm [21, 22] determined by elastic electron-scattering. According to [10], the field shift can be calculated from

$$E_{\mathrm{FS}} = \left( C^{(0)}_{r^2_{\mathrm{rms}}} + C^{(1)}_{r^2_{\mathrm{rms}}} \frac{\mu}{M} \right) r^2_{\mathrm{rms}}, \tag{2}$$

with $C^{(0)}_{r^2_{\mathrm{rms}}} = 1.5664\,\mathrm{MHz\,fm}^{-1}$ and $C^{(1)}_{r^2_{\mathrm{rms}}} = 4.652\,\mathrm{MHz\,fm}^{-2}$, $\mu$ is the electron reduced mass and $M$ is the nuclear mass. Elastic electron scattering provides reliable nuclear charge radii for

stable isotopes. The uncertainty of the results, however, limits the accuracy with which the radii for heavier lithium isotopes can be determined using isotope shift measurements by optical spectroscopy. Presently, the uncertainty in the transition frequency calculation is twice as large as the total nuclear size contribution. The calculated frequency can be compared with the so-far most accurate 2S–3S transition frequency determination of $\nu_0 = 815\,618\,185(3)$ MHz [23]. The theoretical values [2, 7] agree within the estimated theoretical uncertainties, which are about ten times larger than the experimental uncertainty. If the calculated accuracy can be improved by about two orders of magnitude, a direct determination of the nuclear charge radius from the optical measurements comes into reach. According to (1) and (2), the charge radius can be then calculated from

$$r_{\text{rms}}^2 = \frac{\nu_0 - (E_{\text{NR}} + E_{\text{Rel}} + E_{\text{QED}})}{C_{r_{\text{rms}}^2}^{(0)} + C_{r_{\text{rms}}^2}^{(1)} \frac{\mu}{M}} \ . \tag{3}$$

A total accuracy of $\delta \nu_0 \approx 200$ kHz in the transition frequency measurement and a comparably small uncertainty in the theoretical part $\delta \nu_{\text{Theory}}$ will allow for a determination of the charge radius with an accuracy of

$$\delta r_{\text{rms}} = \frac{1}{2 r_{\text{rms}}} \frac{1}{C_{r_{\text{rms}}^2}^{(0)} + C_{r_{\text{rms}}^2}^{(1)} \frac{\mu}{M}} \sqrt{(\delta \nu_0)^2 + (\delta \nu_{\text{Theory}})^2} \approx 0.038 \text{ fm}, \tag{4}$$

which is comparable to the current uncertainty from electron scattering but relies purely on optical measurements and model-independent atomic theory. A similar approach has been used for hydrogen [24] for which QED calculations and transition frequency measurements have already reached a much higher accuracy.

Here, we report the measurement of a lithium transition frequency with a femtosecond laser frequency comb that could lead to a direct charge radius determination, once theory has reached comparable precision. The accuracy in the 2S–3S transition frequency is improved by one order of magnitude compared to the previous measurement [23].

## 2. Experimental set-up

The 2S–3S two-photon transition was induced in a thermal atomic beam of lithium atoms and the excitation was monitored by resonance ionization spectroscopy followed by single ion detection with a quadrupole mass spectrometer (QMS). For the measurements presented here, two atom sources were used. The first, which is schematically shown in figure 1, was a resistively heated graphite tube loaded with lithium metal. The graphite tube has a diameter of 2 mm, an inner length of 20 mm and it was heated by a current of typically 40 A. The furnace exit was located approximately 30 cm away from the ionization region of a commercial QMS. This ionization region has a cylindrical shape with a 4.5 mm diameter entrance aperture, hence, the atom beam entering the interaction region with the laser beam was collimated to approximately 1°. In a second set of experiments, a dilute solution of lithium nitrate was deposited onto a thin carbon foil located a few millimeters away from the first electrostatic lens. The graphite foil was then heated with a few watts from a $CO_2$ laser focused onto the foil, which raised the foil temperature above $1800\,°C$. The lithium nitrate was reduced and lithium atoms were released from the foil. The atoms left the surface with a $\cos^2$ distribution and entered the interaction region with practically no collimation. This geometry was chosen to have the same conditions as in the isotope shift measurements of radioactive isotopes [12, 15].
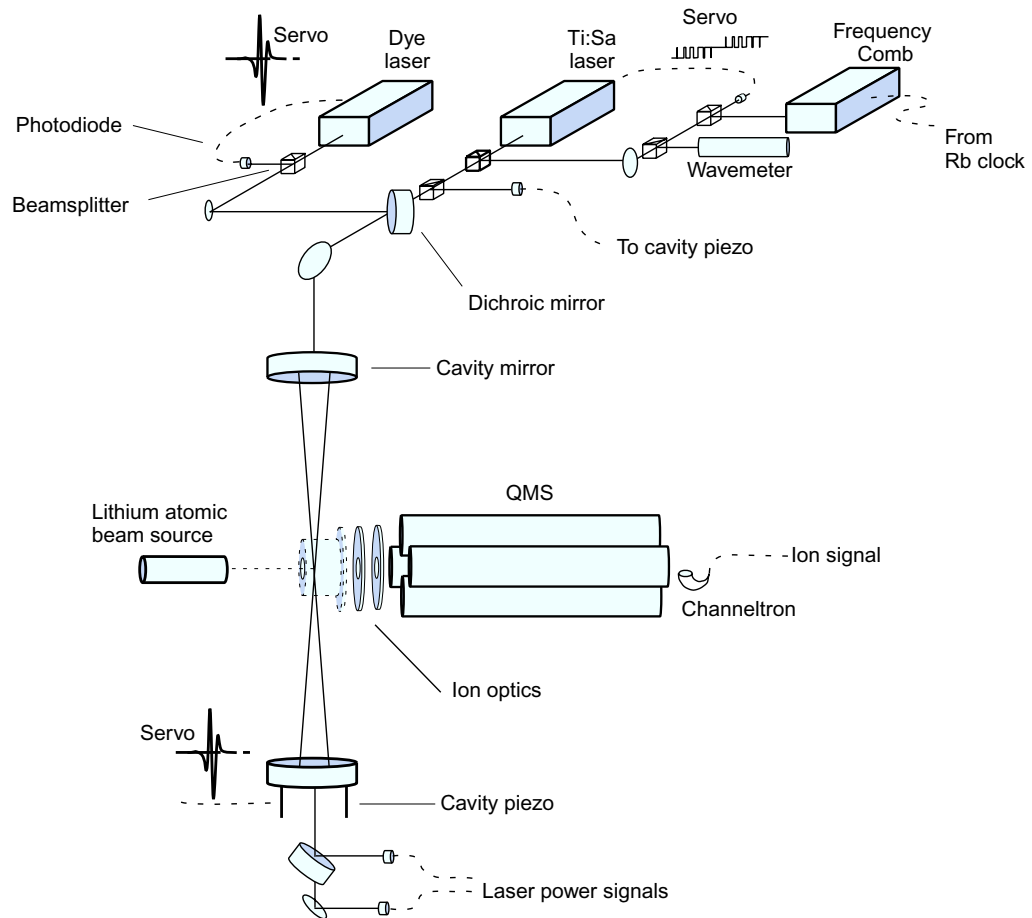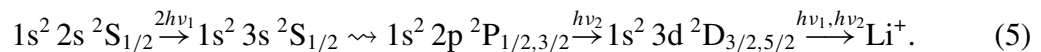
**Figure 1.** Experimental set-up.

The ionization region consists of a small cylinder with two holes on the barrel with about 4 mm in diameter through which the laser beams entered. Atoms crossing this region were excited and ionized by laser light from two lasers with wavelengths $\lambda_1 = 735.1$ nm and $\lambda_2 = 610.5$ nm along the excitation path

$$1s^2\, 2s\ ^2S_{1/2} \overset{2h\nu_1}{\rightarrow} 1s^2\, 3s\ ^2S_{1/2} \rightsquigarrow 1s^2\, 2p\ ^2P_{1/2,3/2} \overset{h\nu_2}{\rightarrow} 1s^2\, 3d\ ^2D_{3/2,5/2} \overset{h\nu_1, h\nu_2}{\longrightarrow} Li^+. \tag{5}$$

The first step is a two-photon excitation followed by spontaneous decay to the 2P level out of which the electron is further promoted via the 3D level into the continuum. Resulting ions were extracted out of the interaction region into the QMS, mass separated and detected with a continuous dynode electron multiplier (CDEM) [25]. The extraction and detection efficiency for the ions was above 50%. Laser light for the two resonant transitions was produced with an argon-ion laser pumped titanium:sapphire (Ti:Sa) laser (Model Coherent 899-21, 735 nm) and a Rhodamine-6G ring dye laser (Coherent 699-21, 610 nm) that was pumped by a frequency-doubled Nd:YVO$_4$ laser (Coherent Verdi-V8). The laser light was transported to the experimental set-up with two single-mode fibers. To produce counter-propagating beams for the two-photon excitation and to obtain the high intensities that are required to drive the two-photon transition, the laser light from the Ti:Sa laser was coupled into a symmetric spherical-mirror optical resonator mounted inside the vacuum chamber. One of the resonator

mirrors was positioned with a piezoelectric transducer and the cavity length was locked to the Ti:Sa laser by the Pound–Drever–Hall (PDH) locking technique [26] to ensure continuous resonance enhancement for all frequencies. Simultaneous enhancement for both laser beams inside the optical resonator was achieved by combining the beams with a dichroic beamsplitter and locking the dye laser to the optical resonator by controlling its frequency, again using the PDH locking. A small amount of laser light, proportional to the light power circulating within the resonance cavity, exited the cavity through the high-reflector, and left the vacuum chamber through a wedged viewport (to avoid interference effects in measurements of the transmitted laser intensities). It was separated again into the two wavelength components with another dichroic beamsplitter. Each beam was directed onto a photodiode and the photocurrent was recorded to track the laser powers inside the cavity.

The maximum output power of the Ti:Sa (dye) laser was 1200 mW (400 mW) of which up to 900 mW (250 mW) was transported through the fiber. After the optics for phase modulation used for PHD locking, beam shaping for mode matching and dye-Ti:Sa beam overlap, about 600 mW (150 mW) was left at the viewport into the vacuum chamber. With this input power, a power of approximately 40 mW (7 mW) was observed at the photodiode behind the cavity. Spherical cavity mirrors, with 500 mm radius of curvature and spaced by 300 mm, yielded a cavity $g$-parameter of 0.16. The calculated focal spot size at the center of the cavity was 0.46 mm. Combined with the 98% reflectivity of the input mirror and a finesse of 110, the calculated intensity of the Ti:Sa laser beam in the interaction region was roughly 400 W mm$^{-2}$, which is larger than the estimated saturation intensity of $\approx$170 W mm$^{-2}$. For the dye laser a maximum intensity of 74 W mm$^{-2}$ was expected, a value that surpasses the theoretical saturation intensity of $I_{Sat} = \pi hcA_{3D-2P}/\lambda^3 = 0.18$ mW mm$^{-2}$ (where $A_{3D-2P} = 8.653 \times 10^7$ [27] has been used) by orders of magnitude. This leads to strong saturation broadening of the 2P–3D dipole transition such that the fine structure of both levels was covered within the linewidth and an almost constant excitation efficiency was observed over a range of 2 GHz. The ionization step was non-resonant and it was not sensitive to the exact frequencies of the laser.

The Ti:Sa laser was phase-locked to one of the modes of a commercial fiber-laser-based femtosecond frequency comb (Menlo Systems, Model FC 1500). The erbium-doped fiber laser was operated at a wavelength of approximately 1560 nm and a frequency comb in the red and near infrared region was produced by frequency doubling and subsequent spectral broadening in a nonlinear fiber. The laser repetition rate, $\nu_{rep}$, of approximately 100 MHz was stabilized by comparing the output of a radio frequency (RF) generator (Stanford Research Systems, Model SRS 543) with the difference between the 98th harmonic of the 10 MHz output of a rubidium clock (Stanford Research Systems, Model FS 725) and the 10th harmonic of the repetition rate that was recorded with a fast photodiode. By varying the SRS frequency between 19 and 21 MHz the repetition rate of the laser was chosen between 99.9 and 100.1 MHz. The beat signal, $\nu_{Beat}$, between the Ti:Sa laser and the nearest comb mode was detected with a fast photodiode and stabilized to an offset frequency of 30 MHz with a digital phase-lock system (Menlo Systems, FCX 200). The servo signal for the stabilization of the Ti:Sa-laser was applied to the external-scan input of the Coherent 899-21 controller. This limited the servo bandwidth to approximately 100 Hz but the fast internal stabilization of the Ti:Sa laser to its reference cavity reduced the laser linewidth to about 1 MHz. Once the Ti:Sa laser frequency was locked to the $n$th comb mode it was calculated according to

$$\nu_{Ti:Sa} = n \times \nu_{rep} \pm 2 \times \nu_{CEO} \pm \nu_{Beat}, \tag{6}$$
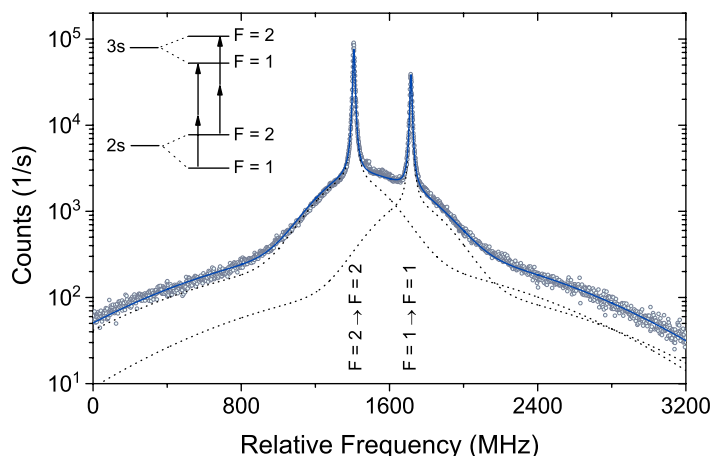
**Figure 2.** Overall lineshape for the 2S–3S two-photon transition in $^7$Li. The Ti:Sa laser frequency is given relative to the frequency comb mode of 407 807 570 MHz. The line is the overall fit to the experimental points (○). The dotted lines are the contributions of the individual peaks.

where $n$ is the number of the comb mode to which the laser was locked. The carrier envelope offset $\nu_{CEO}$ of the femtosecond laser was stabilized to 20 MHz and it was doubled to account for the laser frequency doubling. The Ti:Sa-comb beat frequency $\nu_{Beat} = 30$ MHz was stabilized as described above. The sign of the CEO and beat frequencies were determined experimentally and they were then fixed during the measurements. The mode number $n$ can either be determined from a set of measurements at different repetition rates or by using a lambdameter with a resolution of better than 100 MHz. We have used a Fizeau–Interferometer (ATOS). The Ti:Sa laser frequency can then be tuned in a controlled and precise manner by changing the repetition frequency of the femtosecond fiber laser. Therefore, the frequency of the SRS RF generator was computer controlled via a GPIB interface. Scans of the hyperfine structure of the lithium transitions were recorded by changing the repetition rate in steps of 0.1 Hz. This corresponded to a step width of approximately 410 kHz ($n \approx 4\,100\,000$) in the Ti:Sa laser frequency and, thus, about 820 kHz in the two-photon transition frequency.

The dye laser frequency was tuned close to the resonance of the 2p $^2P_{3/2} \rightarrow$ 3d $^2D_{5/2}$ transition and then locked to the nearest longitudinal mode of the enhancement cavity. Hence, the frequency was not fixed exactly on the resonance transition. However, due to the enhanced power inside the cavity, the transition was broadened to about 10 GHz (full-width at half-maximum (FWHM)) with a flat-top region of 2 GHz. Therefore the exact frequency position as well as the small frequency shift that appears during a scan of the Ti:Sa laser frequency did not have a detectable influence on the transition probability and, hence, on the lineshape of the resonance line.

## 3. Overall spectrum

Figure 2 shows a spectrum recorded for $^7$Li. At the start of the scan, the Ti:Sa was locked to comb mode number 4 078 075 at 100 MHz repetition frequency and both beat note and carrier offset frequency were locked with positive sign, resulting in a total Ti:Sa frequency of 407 807 570 MHz. The scan was performed by increasing the repetition rate in steps of 0.5 Hz

(2.04 MHz of the Ti:Sa frequency) and integrating the ion counts for 1 s at each point. The transition is splitted into two hyperfine components ($I = 3/2$ for $^7$Li) as shown schematically in the inset of figure 2. The selection rules for a $^2$S$_{1/2} \rightarrow \,^2$S$_{1/2}$ transition require $\Delta F = 0$, hence, only two lines were observed.

The centers of the two lines were found by fitting theoretical line profiles to the signal. The fit function was a sum of two Gaussian pedestals, corresponding to Doppler-broadened excitation in the atomic beam (FWHM = 800 MHz) and in the background gas (FWHM = 1.6 GHz), and a Voigt profile for the Doppler-free two photon excitation. The fitting function includes nine free parameters: these are the positions of the two peaks that are also identical with the background Gaussian centers, the Gaussian and Lorentzian widths of the Voigt profiles, the widths of the two background Gaussians, the amplitude of the Voigt profile and the amplitude of the two background Gaussians relative to the Voigt profile intensity. Besides the absolute amplitude of the Voigts and their positions, all parameters were constrained to be identical for both hyperfine components. No additional baseline offsets were used in the fit. The Gaussian backgrounds were both produced by the simultaneous absorption of two co-propagating photons whereas the Doppler-free component arose from the absorption of counter-propagating photons. In previous atomic beam measurements [23], we observed similar spectra but with a much smaller width of only 30 MHz for the stronger Gaussian component. This was attributed to Doppler-broadened excitation of lithium atoms in the well collimated atomic beam. The much larger width observed here was probably due to lower atomic beam collimation and scattering due to the higher background gas pressure. In the present experiment, the atomic beam oven was not operated in a separate chamber with a differential pumping as it was done in [23]. Nonetheless the model function fitted the observed spectrum very well with a reduced $\chi^2 = 1.18$. The Doppler-free peak had a 10.6 MHz (FWHM) Lorentzian component. This was about twice the 5.3 MHz expected from the 29.8 ns lifetime of the 3S level [27, 28], mainly caused by power broadening. The Gaussian component of the Voigt had a width of 4.3 MHz, which was about 3–4 times the laser jitter width of the Ti:Sa laser of about 1.2 MHz.

Once the center of the two hyperfine transitions was obtained, the center of gravity (cg) of the hyperfine structure was calculated according to

$$\nu_{cg} = \tfrac{5}{8}\nu_{F=2\rightarrow F=2} + \tfrac{3}{8}\nu_{F=1\rightarrow F=1} \tag{7}$$

for $^7$Li and

$$\nu_{cg} = \tfrac{2}{3}\nu_{F=3/2\rightarrow F=3/2} + \tfrac{1}{3}\nu_{F=1/2\rightarrow F=1/2} \tag{8}$$

for $^6$Li, respectively.

## 4. Skip-step scans

To obtain better statistics for the determination of peak positions, skip-step scans were used as shown in figure 3. High-resolution scans were recorded in a 30 MHz frequency window around each resonance with steps of 0.8 MHz while inter-peak regions were scanned quickly without data acquisition (skipped steps). Figure 3 shows spectra for two different Ti:Sa laser powers: (a) 100% and (b) 25% of the maximum power available. The solid line represents the overall fitting function that includes the Gaussian backgrounds with linewidth parameters fixed at values obtained from the overall spectrum in figure 2. The intensity of the Doppler-free components, their Gaussian and Lorentzian Voigt component widths and their amplitudes relative to the Doppler-broadened Gaussian background were used as fitting parameters.
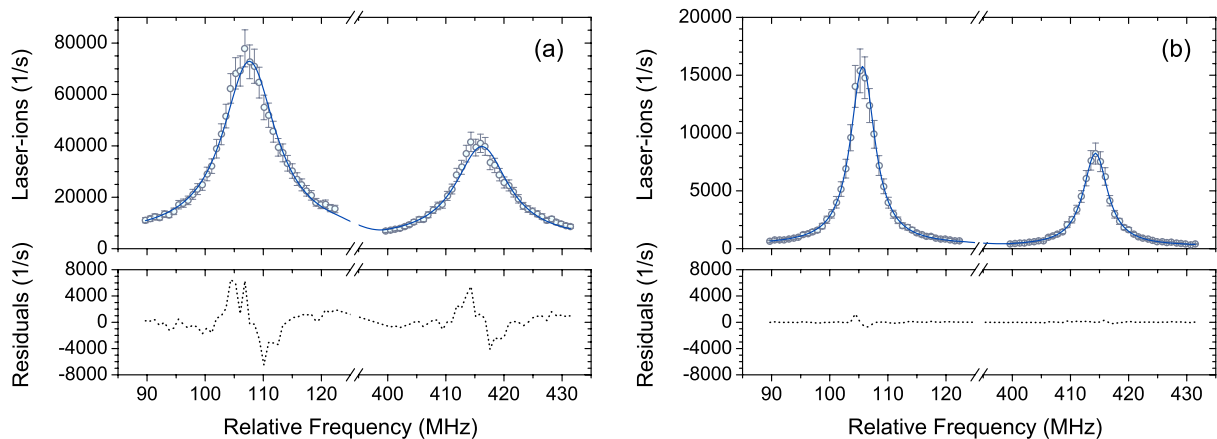
**Figure 3.** Skip-step scans of $^7$Li for Ti:Sa laser intensity of (a) $430\,\mathrm{W\,mm}^{-2}$ and (b) $110\,\mathrm{W\,mm}^{-2}$. The black lines are the fits while the dotted lines show the behavior of the residuals. The frequency axes are relative to the start frequency of the scan of $407\,808\,870\,\mathrm{MHz}$.

Below each resonance, the residual between the experimental data and the fitted function are shown. An asymmetry of the recorded spectrum, that is not reproduced by the fitting function, can be clearly observed, particularly at high laser power (a). We tested whether this effect could be caused by an asymmetry of the Gaussian pedestal which could arise from a misalignment of the atomic beam, but we found that the asymmetry was too strong to arise from the weak background. Moreover, the strong power dependence would not be expected in this case. We assume that the asymmetry is caused by a spatially dependent ac-Stark shift as will be discussed below.

Skip-step spectra like those shown in figure 3 were recorded for varying intensities of the Ti:Sa and of the dye lasers. The observed resonances were fitted and the center of gravity of the hyperfine structure was calculated. Figure 4 shows the measured centers of gravity as a function of the Ti:Sa laser power measured behind the cavity. During these measurements the dye laser power was kept constant. The data points are well described by a linear function, as expected for an ac-Stark shift with the lasers far-off resonance for all dipole transition involving the 2S or 3S levels. The extrapolated frequency at zero laser power is the resonance frequency unperturbed by the Ti:Sa laser field. To eliminate similar ac-Stark shifts from the dye laser, we plotted all measurements with varying dye and Ti:Sa laser powers three-dimensionally and fitted a plane to the data points. In this way the actual laser power in each measurement can be directly plotted and small drifts of the dye laser power during an ac-Stark shift measurement with the Ti:Sa laser do not influence the result. The data points and the fitted plane are shown in figure 5.

Typically we used about 50 measurements for a single extrapolation to the intercept frequency at the point of zero dye and Ti:Sa intensities. Reduced $\chi^2$ of these fits were between 1 and 5 and the uncertainties obtained from the fitting routine were scaled with the square root of $\chi^2_{\mathrm{red}}$. We have recorded about 150 spectra for $^7$Li over three days with both types of atom sources (see section 2). Those were combined to three data sets for extrapolation of the resonance frequency. No systematic offset between the oven and foil measurements was observed and all values agreed well within their uncertainties. The weighted average of the results is $815\,618\,181.735\,(71)\,\mathrm{MHz}$. For $^6$Li, measurements were also carried out with both
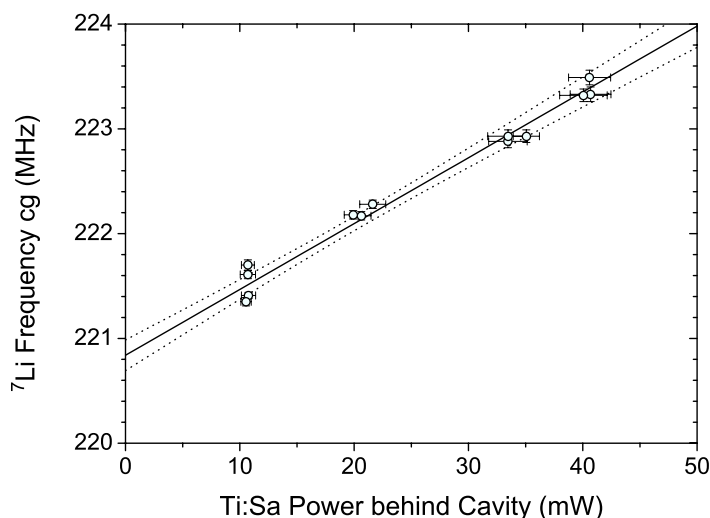
**Figure 4.** Ac-Stark shift for $^7$Li two-photon transition as a function of the power of the Ti:Sa laser. The frequency axis is relative to the start frequency as given for figure 3. The centers of gravity of the hyperfine structure splitting (○) are fitted with a linear function (solid line) $\nu_{cg} = b_0 + b_1 P_{Ti:Sa}$, where $b_0 = 220.84(7)$ MHz and $b_1 = 0.062(3)$ MHz mW$^{-1}$. If the intensity inside the cavity is used, $b_1$ changes to $b_1$(intracavity) $= 0.0058(3)$ MHz W$^{-1}$ mm$^2$. The upper and lower 95% confidence levels are represented by the dotted lines.
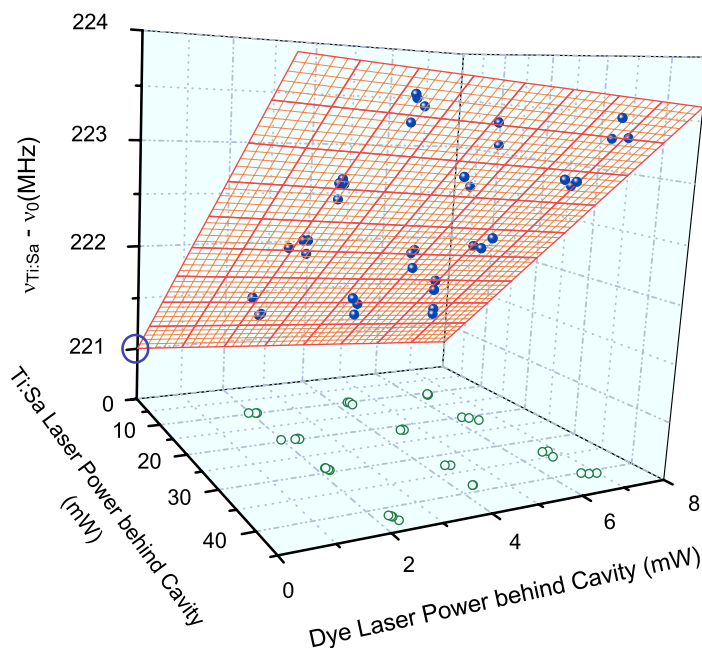


**Figure 5.** Two-dimensional plot of the ac-Stark shift. The filled points are the experimental data and the open circles are the projection of these points on the $x$–$y$ plane. The shaded plane is the two-dimensional fit: $\nu_{cg} = B_0 + B_1 P_{Ti:Sa} + B_2 P_{Dye}$. $B_0 = 220.93(5)$ MHz, $B_1 = 0.065(1)$ MHz mW$^{-1}$, and $B_2 = -0.024(8)$ MHz mW$^{-1}$ (in terms of the laser intensity inside the cavity $B_1 = 0.0061(1)$ MHz W$^{-1}$ mm$^2$, and $B_2 = -0.0022(8)$ MHz W$^{-1}$ mm$^2$).

atom sources and about 90 spectra were taken and separated into two sets. Statistical precision of fitting the resonance signal was worse due to the $\approx 7\%$ abundance of $^6$Li in the natural abundance samples used for the measurements. In combination this led to a larger overall uncertainty and a value of $815\,606\,727.882\,(180)\,\text{MHz}$ was obtained. The isotope shift taken as a difference between these two absolute frequencies is $\Delta\nu_{\text{IS}} = 11\,453.85\,(19)\,\text{MHz}$, which is in good agreement with the more accurate value of $11\,453.984\,(20)\,\text{MHz}$ obtained from relative measurements [15].

## 5. Line profile modeling

To estimate the influence of the residual asymmetry (figure 3) on the line center frequencies we had first to understand its origin. Atoms that are not passing through the center of the laser beam experience lower intensities and, thus, smaller ac-Stark shifts. The effect is not symmetric since all atoms passing through the wings are shifted to one side of the resonance. The center region has the highest intensity and therefore the highest ionization efficiency but also the largest ac-Stark shift. Atoms traversing the wings of the laser beam have a smaller ionization efficiency but they are in resonance at lower frequencies since the ac-Stark shift (due to the Ti:Sa laser) increases the resonance frequency. Thus, they appear on the lower frequency side of the resonance curve and the corresponding intensity above the resonance is missing. A similar effect is caused by laser intensity fluctuations that occur due to changes in the length of the enhancement cavity that are too fast to be completely compensated by the locking servo loops. Again, the signal is shifted into the frequency range below the resonance frequency observed at highest cavity power. To quantitatively understand whether these effects distort the line profile in the observed way, we performed simulations of the ionization process in the laser fields.

### 5.1. The model

To understand the line profile we have used a rate equation model to calculate the time-varying ionization efficiency of atoms passing the laser beam at different positions. A scheme of the simplified excitation ladder that has been used is shown in figure 6(a). The two-photon transition rate as a function of laser intensity is given by

$$W_{12} = \frac{I^2}{I_\text{S}^2} \frac{A_{23}^2}{4} \frac{A_{23}}{4\delta\omega^2 + A_{23}^2/4}, \tag{9}$$

with the on-resonance transition rate $W_{12}(\delta\omega = 0) = (I^2/I_\text{S}^2)A_{23}$, $A_{23} = 1/\tau_{3\text{s}} = 33\,\text{MHz}$ and $I_\text{S} = 167\,\text{W\,mm}^{-2}$ being the total Einstein $A$ coefficient between the 3S and 2P levels and the saturation intensity for the two-photon transition, respectively. $I_\text{S}$ has been experimentally determined from the dependence of the linewidth on the laser intensity. This simplified transition rate for the two-photon transition fulfills the following conditions for the lineshape: (a) at low laser intensity we observe a Lorentzian with a width of $A_{23}$, (b) with increasing intensity the transition rate increases proportional to the square of the intensity, (c) at the saturation intensity $I = I_\text{S}$ the pump rate at resonance is as large as the relaxation rate and (d) the linewidth increases with intensity according to $(1 + (I/I_\text{S})^2)^{1/2}$. It may be noted that it is not necessary to distinguish between the decay into the two fine structure levels 2P$_{1/2}$ and 2P$_{3/2}$ since both have the same probability of being ionized as well as for decay back into the 2S$_{1/2}$ ground state. The latter has
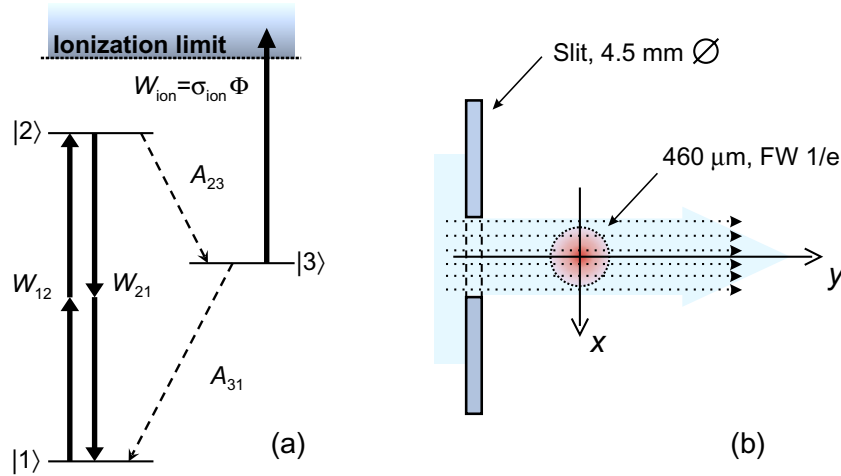
**Figure 6.** Schematic representation of (a) the excitation ladder used in the model, and (b) a collimated atomic lithium beam passing through a Gaussian laser field distribution.

a transition rate of $A_{31} = 1/\tau_{2p} = 37\,\text{MHz}$ (see table 2). The rate equations for excitation and ionization are then given by

$$\dot{N}_1 = W_{12}(N_2 - N_1) + A_{31}N_3,$$
$$\dot{N}_2 = W_{12}(N_1 - N_2) - A_{23}N_2, \tag{10}$$
$$\dot{N}_3 = A_{23}N_2 - A_{31}N_3 - \sigma_{\text{Ion}}\Phi N_3,$$

with the photon flux $\Phi = I_{\text{Laser}}/h\nu$ of the ionization laser and the ionization cross section $\sigma_{\text{Ion}}$. $N_1$, $N_2$ and $N_3$ are the populations of the 2S, 3S and 2P levels, respectively, and $N_{\text{tot}} = N_1 + N_2 + N_3$ is the total number of neutral atoms. Now we add the effect of the laser ionization onto the population

$$\dot{N}_{\text{Ion}} = -\dot{N}_{\text{tot}} = \sigma_{\text{Ion}}\Phi N_3. \tag{11}$$

The numerical integration of these coupled differential equations was performed using an adaptive-step-size 4th order Runga–Kutta algorithm taken from [29]. We have taken into account the laser intensity profile, the displacement along $x$ from the center of the laser beam, and the velocity distribution within the atomic beam. The assumed geometry is shown in figure 6(b): a 4.5 mm diameter hole is used to collimate the atomic beam from the graphite oven; 6 mm behind the aperture the atoms cross the laser beam in the relatively soft focus of the enhancement cavity with a full width 1/e diameter of 460 $\mu$m.

The Gaussian intensity distribution of the laser beams has two effects on the interaction: (i) regarding the reference frame of the atomic beam in the longitudinal direction, the atom experiences a continually changing intensity, hence varying $W_{12}$ values and ionization rates as it passes through the laser beams; (ii) in the transverse dimension, some atoms pass through a region off-center of the laser beams and encounter overall reduced intensities. The longitudinal distribution is easily accounted for by using an appropriate time-space transformation for the given atomic velocity. In this way, the $W_{12}$ value and the photon flux $\Phi$ responsible for the two-photon excitation and ionization rates during the numerical integration are continuously adjusted. In contrast, the transverse dimension requires adding another dimension to the overall

**Table 2.** Typical parameters used in the simulations.

| Parameter | Symbol | Value | Unit | Reference |
|---|---|---|---|---|
| Full decay rates | $A_{23}$ | 33.0 | MHz | [28] |
| | $A_{31}$ | 7.0 | MHz | [28] |
| Laser wavelength | $\lambda$ | 735.0 | nm | |
| Two-photon saturation intensity | $I_S$ | 167 | W mm$^{-2}$ | [31] |
| Ionization cross section | $\sigma_{ion}$ | $2 \times 10^{-15}$ | cm$^2$ | This work |
| Ac-Stark shift coefficient | $a_{ac-Stark}$ | Variable | MHz mW$^{-1}$ | This work |
| Laser beam waist (1/e) | $w_{laser}$ | 460 | $\mu$m | [31] |
| Temperature | $T$ | 2000 | K | This work |

integration procedure. Integration over the spatial displacement in the $x$-direction and the velocity distribution was performed as a discrete summation, typically over 19 and 40 segments, respectively. The atomic beam intensity distribution along $x$ was assumed to have a rectangular profile limited by sharp mechanical apertures. The velocity distribution was assumed to be Maxwell–Boltzmann for the thermal source. When expressed as the flux distribution in an atomic beam, it is given by [30]

$$\Phi_{\text{Atoms}}(\upsilon) = 2\alpha^{-4}\upsilon^3 \exp\left(-\upsilon^2/\alpha^2\right) \, \mathrm{d}\upsilon, \tag{12}$$

where $\alpha = \sqrt{2kT/m}$ is the most probable velocity. The integration was carried out up to $4\alpha$ where the relative flux dropped to $2 \times 10^{-5}$ of the maximum. To avoid artificial intensity oscillations that can occur when discrete velocity segments are taken in regular increments, a quasi Monte-Carlo approach was used. At each position-velocity step the particular values were randomized within the range of $\pm\mathrm{d}x/2$ and $\pm\mathrm{d}\upsilon/2$, where $\mathrm{d}x$ and $\mathrm{d}\upsilon$ are the summation step sizes. For the laser's Gaussian intensity profiles, integration was carried out over four times the FWHM of the beam diameter corresponding to points where the intensity has dropped off to $10^{-4}$ of the maximum value.

In equation (9), the effect of power broadening for the transition line profile is included. However, the ac-Stark effect is not taken into account. This effect is caused by non-resonant interaction of the S levels with all available P levels in the atom in the presence of strong laser fields. To artificially include the effect in the model, we consider in $\delta\omega = 2\pi\delta\nu$ not only the usual detuning of the laser frequency $\Delta\nu_{\text{Laser}}$ but also the additional linear ac-Stark shift

$$\delta\nu = \Delta\nu_{\text{Laser}} - a_{ac-\text{Stark}}I(x, y, t) \tag{13}$$

and replace the term $\delta\omega$ in (9) with this position-dependent function. The value of the linear ac-Stark shift coefficient $a_{ac-\text{Stark}}$ was adjusted to obtain the experimentally observed ac-Stark shift depicted in figure 4. Fast intensity fluctuations on a timescale of a few $\mu$s due to cavity length fluctuations were observed with intensity droppings down to 30% of maximum. To estimate the influence on the line profile, we assumed a sinusoidal behavior for the intensity with a variation of 70% and a frequency of $\sim 30$ kHz. To average over different phases at the time when the atom enters the laser beam, another discrete summation with a step size of $4°$ was carried out, covering the full possible range of $360°$.
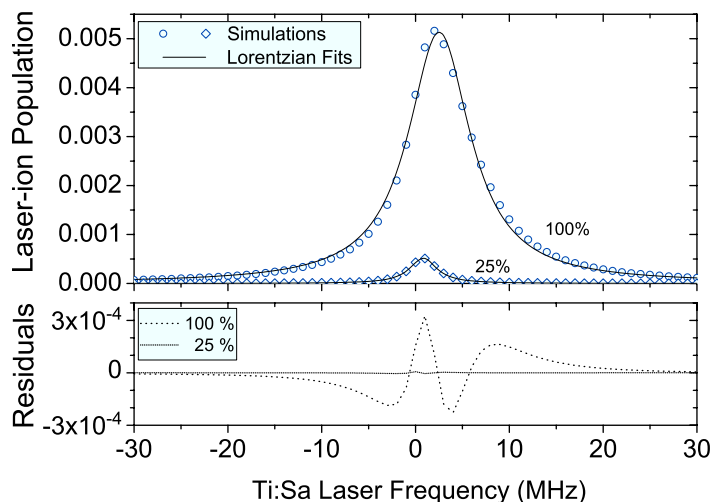
**Figure 7.** Line profile simulation for 'low-power' (25%, equivalent to 110 W mm$^{-2}$) and 'high-power' (100%, equivalent to 430 W mm$^{-2}$).

## 5.2. Results

We will now discuss the results of lineshape calculations. First, the lineshape and the shifts of resonance centers are discussed before we turn to the relevance of these calculations for the determination of the transition frequency.

*5.2.1. Lineshapes.* Figure 7 shows the results of lineshape calculations at typical laser powers used in 'high-power' and 'low-power' measurements. Lorentzian line profiles have been fitted to the simulated data and the residuals between the fit and the simulated data are plotted in the lower part of the figure. The residuals show a similar behavior as in the case of the experimental data (figure 3).

Figure 8 shows the calculated lineshape for different distributions of the laser field: a rectangular profile that has a homogeneous laser intensity distributed all over the area of the laser beam (R), a Gaussian profile with stationary laser power (G) and a Gaussian profile that takes into account the intensity fluctuations of the laser beam (GF). The simulations were performed at the highest laser intensity used experimentally. The most striking difference between the rectangular and Gaussian profiles is the reduction in ionization efficiency and a shift of the resonance center of 1.7 MHz in the case of the Gaussian profile. Both effects are caused by the reduction of laser intensity in the non-central region of the laser beam and, hence, the lower excitation efficiencies and ac-Stark shifts. The Gaussian with intensity fluctuations only introduces small differences when compared to the same Gaussian distribution without fluctuations.

*5.2.2. Ac-Stark shift.* Line profiles of the hyperfine transition of $^7$Li were simulated at different laser intensities of the laser field for a Gaussian distribution with intensity fluctuations. From these profiles the peak centers were extracted and the results are plotted in figure 9 as a function of the laser power measured behind the cavity. A linear fit was performed on the region where the experimental data have been obtained (10 mW $\leqslant P_{\text{Ti:Sa}} \leqslant$ 45 mW). At lower laser
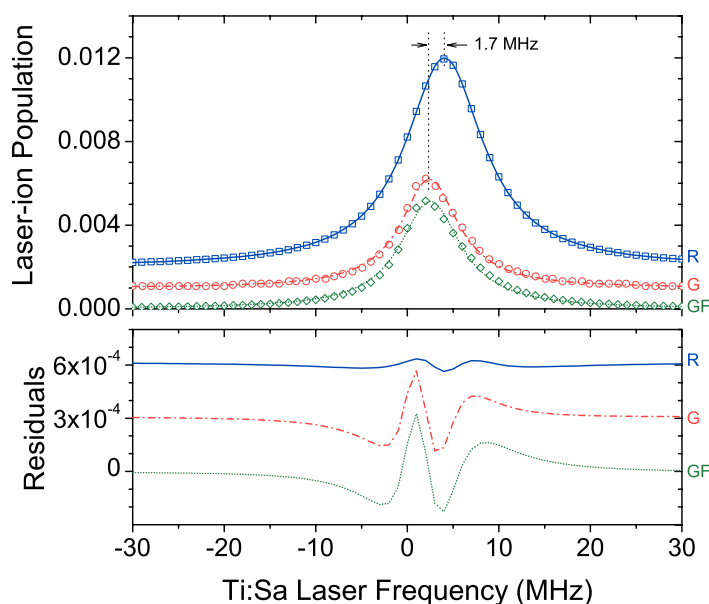
**Figure 8.** Simulation of the line profile for different laser field distributions, R: rectangular, G: Gaussian and GF: Gaussian plus intensity fluctuations. These lineshapes have also been fitted with Lorenztian line profiles and the corresponding residuals are plotted in the lower part of the graph. Line profiles R and G and their residuals have been artificially shifted vertically (offsets of $10^{-3}$ and $3 \times 10^{-4}$, respectively) in order to be distinguished from each other.

intensities, the simulated data smoothly move away from the linear behavior approaching zero. By considering only a linear ac-Stark shift, a systematic shift of 170 kHz is introduced in the determination of the peak center. Such a deviation is not observed if we assume a rectangular laser beam profile. In this case the linear behavior continues and by extrapolation the correct frequency is obtained. Thus, we believe that the additional shift is real and is introduced by the increasing distortion of the peak profile. To estimate the uncertainty of this correction, we have performed similar calculations as shown in figure 9 for various amounts of laser intensity fluctuations (20–80%) since this is the least known parameter in the model. The results span a range of 65 kHz, which has fully been taken as an additional systematic uncertainty.

In the simulation, we have only considered the intensity distribution and fluctuations of the Ti:Sa-laser field: it has considerably higher intensity, is completely responsible for the resonance transition, and represents the dominant source for non-resonant ionization. Moreover, the ac-Stark shift coefficient for the dye laser light extracted from figure 5 is $-0.0022(8)\,\mathrm{MHz\,W^{-1}\,mm^2}$, whereas it is 2.7 times larger for the Ti:Sa laser light ($0.0061(1)\,\mathrm{MHz\,W^{-1}\,mm^2}$).

## 6. Summary of systematic uncertainties

Table 3 shows statistical and systematic errors that contributed to the overall uncertainty of the 2S–3S transition frequency of $^7$Li. The statistical uncertainty is given as the standard deviation of the individual results. A systematic error that has to be taken into account is the uncertainty
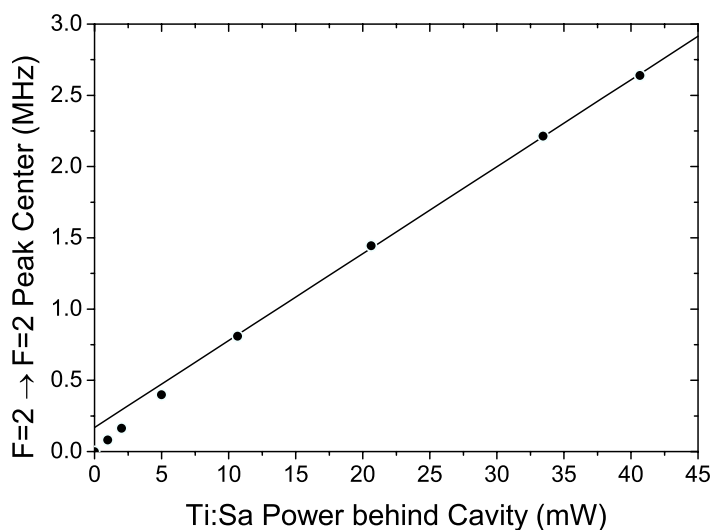
**Figure 9.** Simulation of a one-dimensional ac-Stark shift (full dots). The solid line ($y = 0.167 + 0.061x$) is a linear fit to the data between $10\,\text{mW} \leqslant P_{\text{Ti:Sa}} \leqslant 45\,\text{mW}$.

**Table 3.** Summary of statistical and systematic uncertainties of the absolute transition frequencies in $^{6,7}\text{Li}$. All values are in kHz.

|  | $^7\text{Li}$ | $^6\text{Li}$ |
|---|---|---|
| Statistical | 71 | 180 |
| Systematic |  |  |
|     Frequency comb | 143 | 143 |
|     Ac-Stark shift | 65 | 65 |
|     Zeeman effect | 30 | 30 |
|     Subtotal | 160 | 160 |
| Total | 175 | 241 |

of the rubidium clock (FS725 from Stanford Research Systems) that was used as a reference frequency for the comb. It was calibrated by the manufacturer 256 days ($= 0.701$ years) before and the data were taken during one week. The Rb standard is specified to provide a relative accuracy of better than $\pm 5 \times 10^{-11}$ at the date of calibration and a drift of $<5 \times 10^{-10}\,\text{year}^{-1}$. The relative uncertainty of the Rb frequency standard at the time of the measurement, and therefore of the frequency comb, was taken as the time since calibration multiplied by the yearly drift which amounts to $3.5 \times 10^{-10}$. To obtain the uncertainty of the laser frequency, this relative uncertainty was multiplied by the comb mode number that we have been using. This is 4 078 088 times the repetition rate $\nu_{\text{rep}} = 100\,\text{MHz}$, and therefore $\Delta\nu_{\text{Comb}} = 143\,\text{kHz}$. As discussed in section 5.2 the only other significant systematic uncertainty is that caused by the asymmetric line profile.

The effect of unresolved Zeeman splitting caused by stray magnetic fields was estimated to be less than 30 kHz for both isotopes. The strongest effect would be expected from the magnetic field induced by the current through the graphite crucible. However, a systematic offset between measurements with the oven and foil was not observed.

**Table 4.** Experimental (e) and theoretical (th) values on the $2s\,^2S_{1/2} - 3s\,^2S_{1/2}$ transition frequencies of $^7$Li and $^6$Li. The values of this work contain a $-170$ kHz correction to account for the ac-Stark shift effect, which is discussed in section 5.2.2. The value of $^6$Li given in the last row was obtained by combining the $^7$Li value of this work and the measured isotope shift given in table I of [15].

| | | Reference | Year | Energy (cm$^{-1}$) | Frequency (MHz) |
|---|---|---|---|---|---|
| $^7$Li | e | Radziemski *et al* [32] | 1995 | 27 206.0952 ± 0.0010 | 815 618 215 ± 30 |
| | th | Yan and Drake [6] | 2002 | 27 206.0924 ± 0.0039 | 815 618 131 ± 117 |
| | e | Bushaw *et al* [23] | 2003 | 27 206.0942 ± 0.0001 | 815 618 185 ± 3 |
| | th | Yan and Drake [10] | 2003 | 27 206.0926 ± 0.0009 | 815 618 137 ± 27 |
| | e | This, I$_2$-line [33] | 2004 | 27 206.094 04 ± 0.000 09 | 815 618 180.5 ± 2.7 |
| | th | Yan *et al* [7] | 2008 | 27 206.0936 ± 0.0010 | 815 618 166 ± 30 |
| | th | Puchalski and Pachucki [2] | 2008 | 27 206.0937 ± 0.0006 | 815 618 170 ± 19 |
| | e | This work | 2009 | 27 206.094 082 ± 0.000 006 | 815 618 181.57 ± 0.18 |
| $^6$Li | e | Radziemski *et al* [32] | 1995 | 27 205.7129 ± 0.0010 | 815 606 754 ± 30 |
| | th | Yan and Drake [6] | 2002 | 27 205.7104 ± 0.0039 | 815 606 678 ± 117 |
| | e | Bushaw *et al* [23] | 2003 | 27 205.712 14 ± 0.000 10 | 815 606 731 ± 3 |
| | th | Yan and Drake [10] | 2003 | 27 205.7105 ± 0.0009 | 815 606 683 ± 27 |
| | e | This, I$_2$-line [33] | 2004 | 27 205.711 98 ± 0.000 09 | 815 606 726.6 ± 2.7 |
| | th | Yan *et al* [7] | 2008 | 27 205.7115 ± 0.0010 | 815 606 712 ± 30 |
| | th | Puchalski and Pachucki [2] | 2008 | 27 205.7117 ± 0.0006 | 815 606 717 ± 19 |
| | e | This work | 2009 | 27 205.712 014 ± 0.000 008 | 815 606 727.71 ± 0.24 |
| | e | Direct meas. $^7$Li + IS [15] | 2009 | 27 205.712 013 ± 0.000 006 | 815 606 727.59 ± 0.18 |

## 7. Results and discussion

Table 4 and figure 10 show those experimental and theoretical frequency values of the 2S–3S transition, which have been obtained within the last two decades. The 175 kHz total uncertainty value of our measurement is the quadratic sum of the statistical and systematic uncertainties.

Our experimental value given for the year 2004 was not published independently. We previously reported isotope shift measurements that were referenced to a diode laser locked to a saturated absorption signal of the hyperfine component of the molecular iodine spectrum [12]–[14]. Since then, the absolute frequency of the I$_2$-stabilized diode laser has been measured with the frequency comb [33]. These were then combined to calculate the absolute transition frequency of the 2S–3S transition of the stable lithium isotopes. The uncertainty was in this case dominated by the fact that we used a different laser and stabilization system for the iodine measurements and an additional but stable offset frequency was found. Therefore, a systematic uncertainty of about 3 MHz for the exact locking point of the diode laser system had to be added.

There is still a discrepancy between theory and experiment. Presently the calculations of the absolute transition frequencies on lithium and helium have been performed up to QED terms of order $\alpha^3$ Ry. Calculation for higher order terms of $\alpha$ up to $\alpha^5$ Ry are partially available [2] but they are still not complete and they are the main remaining source of uncertainty for
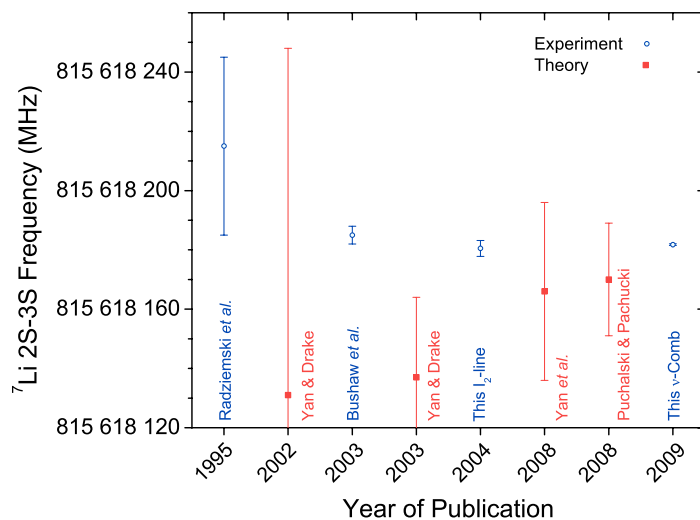
**Figure 10.** Theoretical and experimental transition frequency values of $^7$Li in the 2s $^2$S$_{1/2}$–3s $^2$S$_{1/2}$ transition.

the theoretical energy values given in Table 4. Presently, two groups are working on the theoretical evaluation of the absolute transition for lithium and helium and we hope that accuracy comparable to the experiment will be reached in the future.

## 8. Conclusions

Two-photon laser spectroscopy and resonance ionization together with accurate frequency determination via the frequency comb have allowed us to measure the absolute transition frequencies of the 2S–3S transition of the stable lithium isotopes $^7$Li and $^6$Li with an accuracy of $2 \times 10^{-10}$. The values obtained for $^7$Li and $^6$Li are in agreement with previous results [23] but one order of magnitude more accurate. The new results still disagree by about 12 MHz with the latest theoretical values obtained in [2] which are about 100 times less accurate than the experimental values obtained here. Once the theoretical calculation of the 2S–3S transition energies can be improved by these two orders of magnitude, the extraction of the nuclear charge radii of the lithium isotopes will be possible. Besides the transition reported here, further high accuracy measurements of the $2\,^3$S$_1 \rightarrow 2\,^3$P$_{0,1,2}$ transition in the two-electron system Li$^+$, as have already been obtained at the test storage ring (TSR) at Heidelberg [34] and are under preparation at the MPQ in Garching, would independently facilitate the absolute charge radius determination.

### Acknowledgments

**IOP** Institute of Physics ⚽ DEUTSCHE PHYSIKALISCHE GESELLSCHAFT

# References

[1] Puchalski M, Moro A M and Pachucki K 2006 *Phys. Rev. Lett.* **97** 133001
[2] Puchalski M and Pachucki K 2008 *Phys. Rev.* A **78** 052511
[3] Drake G W F and Yan Z-C 1992 *Phys. Rev.* A **46** 2378
[4] Yan Z-C and Drake G W F 1995 *Phys. Rev.* A **52** 3711
[5] Yan Z-C and Drake G W F 2000 *Phys. Rev.* A **61** 022504
[6] Yan Z-C and Drake G W F 2002 *Phys. Rev.* A **66** 042504
[7] Yan Z-C, Nörtershäuser W and Drake G W F 2008 *Phys. Rev. Lett.* **100** 243002
[8] Drake G W F and Swainson R A 1990 *Phys. Rev.* A **41** 1243
[9] Drake G W F and Goldman S P 1999 *Can. J. Phys.* **77** 835
[10] Yan Z-C and Drake G W F 2003 *Phys. Rev. Lett.* **91** 113004
[11] Pachucki K and Komasa J 2004 *Phys. Rev. Lett.* **92** 213001
[12] Ewald G *et al* 2004 *Phys. Rev. Lett.* **93** 113002
[13] Ewald G *et al* 2005 *Phys. Rev. Lett.* **94** 039901
[14] Wang L-B *et al* 2004 *Phys. Rev. Lett.* **93** 142501
[15] Sánchez R *et al* 2006 *Phys. Rev. Lett.* **96** 033002
[16] Müller P *et al* 2007 *Phys. Rev. Lett.* **99** 252501
[17] Nörtershäuser W *et al* 2009 *Phys. Rev. Lett.* **102** 062503
[18] Žáková M, Geppert C, Herlert A, Kluge H-J, Sánchez R, Schmidt-Kaler F, Tiedemann D, Zimmermann C and Nörtershäuser W 2006 *Hyperfine Interact.* **171** 189
[19] Nakamura T *et al* 2006 *Phys. Rev.* A **74** 052503
[20] Drake G W F 2009 private communication
[21] de Jager C W, de Vries H and de Vries C 1974 *At. Data Nucl. Data Tables* **14** 479
[22] Suelzle L R, Yearian M R and Crannell H 1967 *Phys. Rev.* **132** 992
[23] Bushaw B A, Nörtershäuser W, Ewald G, Dax A and Drake G W F 2003 *Phys. Rev. Lett.* **91** 043004
[24] Udem T, Huber A, Gross B, Reichert J, Prevedelli M, Weitz M and Hänsch T W 1997 *Phys. Rev. Lett.* **79** 2646
[25] Nörtershäuser W *et al* 2003 *Nucl. Instrum. Methods Phys. Res.* B **204** 644
[26] Drever R W P, Hall J L, Kowalski F V, Hough J, Ford G M, Munley A J and Ward H 1983 *Appl. Phys.* B **31** 97
[27] Godefroid M, Fischer C F and Jönsson P 2001 *J. Phys. B: At. Mol. Opt. Phys.* **34** 1079
[28] Froese Fischer C, Saparov M, Gaigalas G and Godefroid M 1998 *At. Data Nucl. Data Tables* **70** 119
[29] Press W H, Teukolsky S A, Vetterling W T and Flannery B P 1996 *Numerical Recipes in C* (Cambridge: Cambridge University Press)
[30] Kusch P and Hughes V W 1959 *Atomic and Molecular Beam Spectroscopy, Handbuch der Physik* Part 1 (Berlin: Springer)
[31] Ewald G 2005 *Messung der Ladungsradien der radioaktiven Lithium-Isotope Li-8 und Li-9* (Heidelberg: Ruprecht-Karls-Universität Heidelberg) pp 52, 73
[32] Radziemski L J, Engleman R Jr and Brault J W 1995 *Phys. Rev.* A **52** 4462
[33] Reinhardt S *et al* 2007 *Opt. Commun.* **274** 354
[34] Reinhardt S *et al* 2007 *Nat. Phys.* **3** 861